Journal of Volcanology and Geothermal Research 468 (2025) 108448

Contents lists available at ScienceDirect

Journal of Volcanology and Geothermal Research

journal homepage: www.journals.elsevier.com/journal-of-volcanology-and-geothermal-research

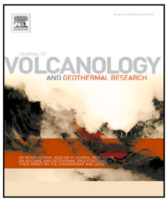

Seismic imaging of mid-crustal heterogeneity beneath geothermal systems, central Taupō Volcanic Zone, New Zealand

Stephen Bannister [a,*], Edward A. Bertrand [b], Geoff Kilgour [c], T. Grant Caldwell [b], Isabelle Chambefort [c], Wiebke Heise [b], Sandra Bourguignon [b]

[a] GNS Science, Avalon, 5040, New Zealand
[b] Earth Sciences New Zealand, formerly GNS Science, Avalon, 5040, New Zealand
[c] Earth Sciences New Zealand, formerly GNS Science, Wairakei research centre, Taupo, 3352, New Zealand

ARTICLE INFO

Dataset link: http://www.geonet.org.nz, https://github.com/nephets-b/2025_seismic_imaging

Keywords:
Geothermal systems
Seismic tomography
Magmatic system
Brittle–ductile
Taupō Rift zone

ABSTRACT

The Taupō Volcanic Zone (TVZ) in New Zealand is a region of highly productive Quaternary volcanism and high hydrothermal heat flux. We investigate the mid-crustal seismic velocity structure of a region within the central, rhyolitic part of the TVZ encompassing high-temperature geothermal systems (e.g. Wairakei, Rotokawa). Using double-difference tomographic inversion of local earthquake data we derive 3-D models of P-wave velocity (Vp) and Vp/Vs for the subsurface. Both high (> 6.0 km/s) and low (< 5.5 km/s) Vp heterogeneities are seen in the mid-crust between 5 and 11 km depth. Regions with high Vp are interpreted to indicate the presence of solidified, more mafic, material within an otherwise quartzo-feldspathic crust, while regions with low Vp values are inferred to represent bodies of crystal-rich magma with a low melt fraction. Using the new 3-D velocity model we then relocated ~9100 earthquakes recorded between 2009 and 2022. The relocated seismicity is strongly clustered, including in the vicinity of some of the geothermal systems (e.g. Rotokawa) where fluid is currently being extracted for electric-power production. Mid-crustal seismicity is also observed west of the Wairakei geothermal field, as well as along the south-eastern margin of the Ngakuru graben and on the western margin of the Whakamaru caldera. The depth distribution of the highest-quality hypocentres shows that 90% of the seismicity at Rotokawa geothermal field occurs at depths shallower than 5.1 km, consistent with a shallow brittle–ductile transition and the presence of a cooling pluton beneath Rotokawa seen in magnetotelluric data.

1. Introduction

The Taupō Volcanic Zone (TVZ) in New Zealand's North Island, is an active, ~2 Myr old, rifted arc formed in continental crust. At the surface, rifting is marked by a 5-to-20 km wide band of active extensional faulting (Fig. 1) (Villamor and Berryman, 2001; Villamor et al., 2017). Extension rates decrease from ~15 mm/yr in the northern part of the TVZ to less than ~5 mm/yr south of Lake Taupō (Wallace et al., 2004). In the central part of the TVZ, volcanism is dominantly rhyolitic with subordinate dacite, andesite and basalt (Browne et al., 1992; Gamble et al., 1993; Wilson et al., 1995; Cole and Spinks, 2009; Wilson et al., 2009; Barker et al., 2020). North and south of the central, rhyolitic part of the TVZ, the volcanism is dominantly andesitic.

Caldera forming eruptions were exclusively sourced from the central part of the TVZ, typified by the 1.6 Ma Mangakino caldera (Fig. 1a) (the oldest recognised), the ~340 ka Whakamaru caldera (the largest recognised), and the 25.5 ka Taupō caldera (the most recent) (Fig. 1). These, and other caldera forming eruptions, have produced a sequence of voluminous ignimbrites that blanketed the regional landscape. Interspersed between the caldera forming eruptions, volcanism in this part of the TVZ is characterised by relatively minor explosive eruptions and dome building episodes. The TVZ is one of the most active volcanic regions on Earth and a hotspot of geothermal energy production. Volcanic hyperactivity in this part of the TVZ is exemplified by the 28 rhyolitic eruptions at Taupō caldera since the 25.5 ka Oruanui eruption (Wilson, 1993).

Petrologic evidence suggests that central TVZ magmas originate from an extensive, petrologically and geochemically heterogeneous mush zone between ~6–15 km depth (e.g. Smithies et al., 2023, 2024; types B and C of Harmon et al., 2024b), before storage in discrete magma bodies between ~4 and 8 km depth (Bégué et al., 2014; Smithies et al., 2023). Mauriohooho (2023) indicates the additional presence of ephemeral boutique magma systems possibly co-existing alongside the larger reservoirs, while Bindeman (2024) suggests that

---

* Corresponding author.
E-mail address: iceseismic@gmail.com (S. Bannister).

https://doi.org/10.1016/j.jvolgeores.2025.108448
Received 1 March 2025; Received in revised form 12 September 2025; Accepted 14 September 2025

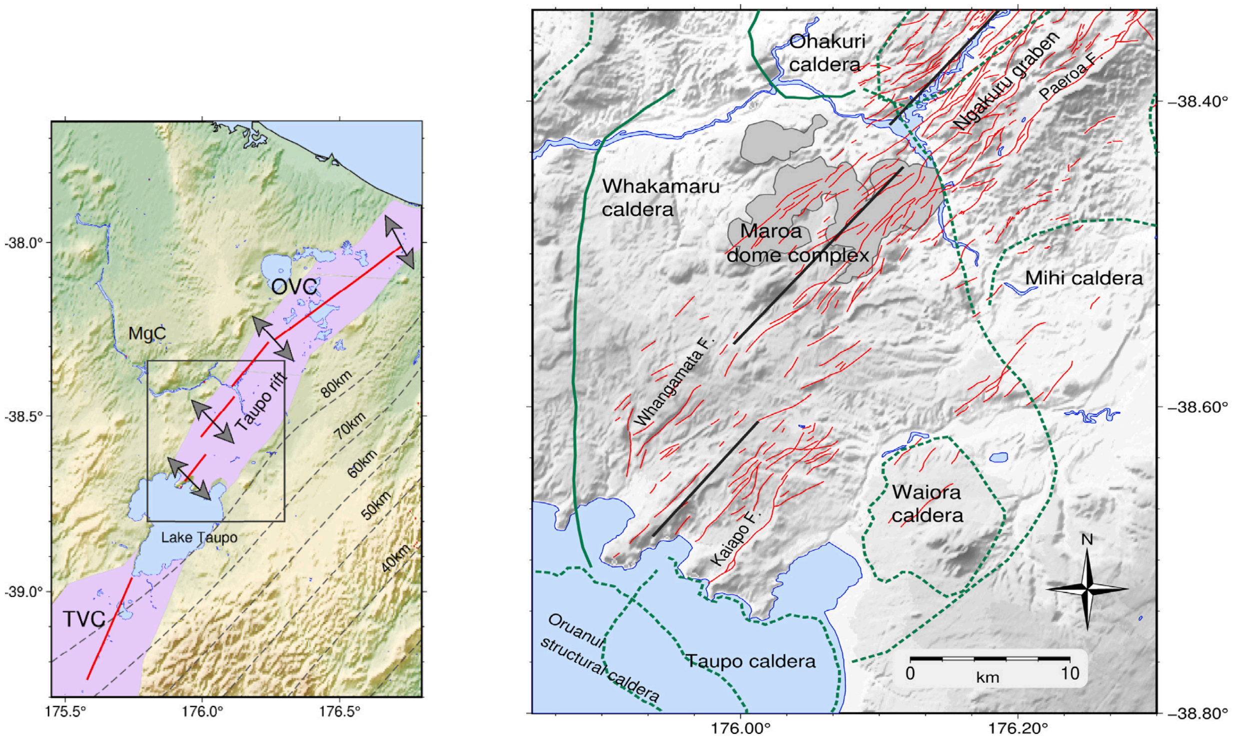

Fig. 1. Left : The Taupo Volcanic Zone, in North Island, New Zealand, with the study region outlined as a box. The Tongariro Volcanic Centre (TVC) and the Okataina Volcanic Centre (OVC) lie to the south and north of the study region, while the Mangakino caldera (MgC) lies to the north-west. The Taupo rift axis is marked as solid red segments, following Seebeck et al. (2014), with extension directions shown as black arrows. Depth contours (km) for the Hikurangi subduction interface are shown as dashed lines, following Williams et al. (2013). Right: Caldera boundaries for Taupo, Whakamaru, Ohakuri, Mihi and Waiora calderas are shown in green, with solid lines when there are surface constraints, dashed lines where caldera boundaries are just inferred (following Rosenberg, 2017; Rosenberg et al., 2019; Stagpoole et al., 2020). Rift axis segments are shown as solid black lines, following Seebeck et al. (2014). Active faults are shown in red, from the New Zealand Active Faults database (Langridge et al., 2016).

rhyolite magmas are stored in a deep crustal melt zone, with limited stagnation in the upper crust.

Magnetotelluric (MT) data has been used to identify a widespread zone of interconnected melt (melt fraction <~4%) beneath the central part of TVZ at ~10 km depth (Heise et al., 2007, 2010). More localised bodies of high electrical conductivity imaged in MT surveys at ~3–7 km depth are interpreted to represent shallower zones of partial melt and/or interconnected saline fluid (Heise et al. 2016, Bertrand et al., 2012, 2015).

The rhyolitic part of the TVZ is also the location of anomalously high heat flux, ~0.7 Wm^{-2}, discharged at the surface in 23 distinct high-temperature geothermal systems (Bibby et al., 1995), (Fig. 2). The high heat flow in the region is inferred to control the shallow (~6 km) seismic–aseismic cutoff depth observed from local seismicity, indicative of the brittle–ductile transition beneath the region (Bibby et al., 1995; Bryan et al., 1999; Ellis et al., 2024).

The petrologic and geochemical studies, as well as the MT data, suggest that considerable spatial heterogeneity of crustal properties is likely in the mid-crust in this part of the TVZ. To date however, there is only sparse information available on spatial variation of seismic properties in the mid-crust beneath the region. Interpretations of 2-D seismic refraction surveys undertaken near Taupō (e.g. Harrison and White, 2004, 2006; Stern and Benson, 2011) suggest that quartzo-feldspathic crust extends to 15–20 km depth. Estimates of seismic properties, such as *P*-wave seismic velocity (*Vp*), *Vp/Vs*, *Qp* and*Qs* derived using previous seismic tomographic inversions of data from local and deeper subduction-zone earthquakes provide information at regional crustal- and upper mantle-scales (Reyners et al., 2006; Eberhart-Phillips et al., 2020), but do not resolve finer-scale mid-crustal heterogeneity.

In this study we investigate *Vp* and *Vp/Vs* structure of the mid-crust of the central part of the TVZ using double-difference seismic tomography (e.g. Zhang and Thurber, 2006), based on observations of the local shallow seismicity. Then, using the new 3-D velocity model, we derive high-resolution locations for more than 9100 shallow earthquakes, which allows us to compare the distribution of seismicity to the mid-crustal *Vp* heterogeneities we observe and to the known geothermal systems.

2. Seismicity detection and location

2.1. Seismic network and data

We use seismic data from earthquakes recorded between 2009 and 2023 by the permanent New Zealand GeoNet seismometer network, supplemented with data recorded by temporary campaign-mode seismometers, as well as data from privately-operated seismometers recording around geothermal reservoirs (Fig. 2). The GeoNet seismometer network (Gale et al., 2015; Petersen et al., 2011) is comprised of permanent broadband and short-period seismometers. In the Taupō region the GeoNet network currently has an average seismometer site spacing of ~15–20 km.

In addition to the GeoNet network seismometers, there have also been various temporary deployments in this region, including the TVZ95 array in 1995 (Bryan et al., 1999; Sherburn and Bibby, 2003), the CNIPSE array in 2001 (Reyners and Stuart, 2002; Reyners et al., 2006; Harrison and White, 2004, 2006) and the HADES array in 2009–2011 (Bannister, 2009). During the temporary array campaigns, the average seismometer spacing in parts of the region was reduced to ~5 km (e.g. during 2001 and 2009–2011). Seismometer site locations for the permanent GeoNet seismometers and the temporary HADES campaign seismometers are shown in Fig. 2. Additional specialised

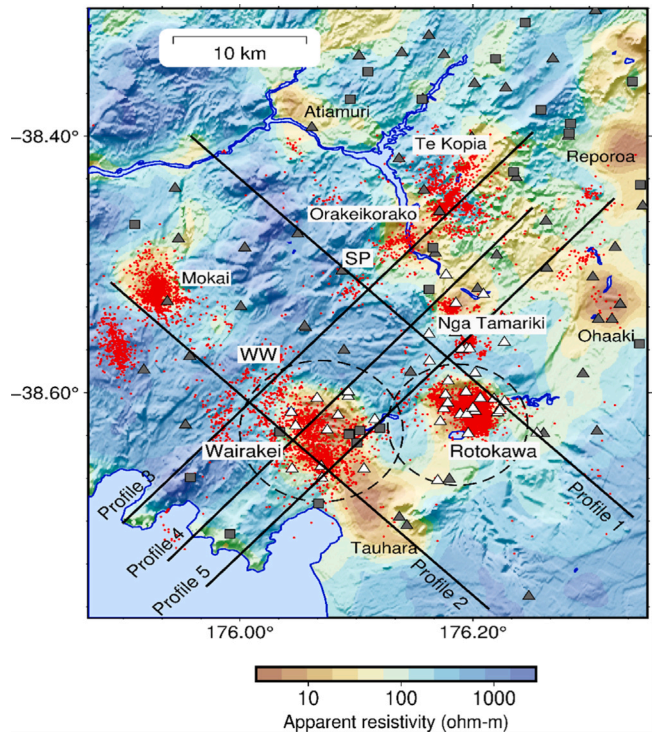

Fig. 2. GeoNet (permanent network) seismometers are shown as filled squares, the temporary HADES campaign seismometers are shown as filled triangles, while privately-operated seismometers around the Wairakei, Rotokawa and Ngā Tamariki geothermal fields are shown as open triangles. Red dots show the epicentres of relocated earthquakes from this study. Solid black lines show the 5 profile lines used for cross-sections in later figures. West Wairakei seismicity:'WW', Southern Paeroa seismicity:'SP', referred to in the text. Dashed circles show the areas used to calculate seismicity ('d90') depth distributions. Background colour shows the DC apparent resistivity (Bibby et al., 1995). Apparent resistivities < 25 Ohm-m provide an indication of the near-surface extent of the geothermal systems (e.g. Rotokawa, Wairakei, Tauhara, Ngā Tamariki, Ohaaki, Atiamuri) in the area shown (see Bibby et al., 1995 for details).

seismic studies have also been carried out to underpin geothermal production field operations in the Wairakei, Rotokawa and Ngā Tamariki geothermal fields (Sherburn et al., 2015a,b; Hopp et al., 2020), some involving borehole seismometers (e.g. Sepulveda et al., 2015).

2.2. Phase picking and initial event location

Phase arrival times of *P* and *S* phases were detected and phase-picked using the machine-learning EQTransformer algorithm and trained model developed by Mousavi et al. (2020). EQTransformer was trained using more than 1 million events from a large range of tectonic environments, but we recognise that future higher-resolution work in our study area might benefit from using ML-models trained with a focus on geothermal seismicity, such as the recent models developed by Okamoto et al. (2024) using Japanese geothermal seismicity. Here we applied EQTransformer to the continuous streams of 3-component data recorded by GeoNet seismometers, as well as to the continuous-stream data recorded by temporary seismometers (e.g. the 2009–2011 HADES array) and reservoir-specific seismometer data.

P and *S* phase arrival picks identified using EQTransformer were subsequently associated into defined events using GaMMA (Zhu et al., 2022), which treats the association as an unsupervised clustering problem in a probabilistic framework. The pick analysis derived a low number of *S*-phase picks, as *S*-wave arrivals in this study area are often obscured by extensive *P*-coda. Such extended *P*-wave coda is likely caused by wave scattering (e.g. Wu and Aki, 1988; Imperatori and Mai, 2015) related to the low velocity volcaniclastic deposits in this region, which may extend to more than 2 kms thickness (e.g Stern and Benson, 2011).

Initial hypocentre locations were subsequently derived using NonLinLoc (Lomax et al., 2000; Lomax, 2005; Lomax et al., 2007), involving a probabilistic non-linear search for hypocentres using the equal differential time likelihood function (Lomax, 2005), based on the approach of Tarantola and Valette (1982). At this stage events were discarded if they had less than 6 phases or an azimuthal gap greater than 300°; the majority of the events had azimuthal gap less than 200°(Supplementary Figure S1).

After this filtering there were 9149 events, which, after further relocation described below, are shown in Fig. 2. Vertical uncertainties in location, found from the projection of the 68% confidence ellipsoids, vary depending on the proximity to nearby seismometers, and on the number of phase-picks; the median of the vertical uncertainty was 2.1 km for the 9149 events (Figure S2), but this does not reflect additional uncertainties due to velocity model errors (Husen and Hardebeck, 2010). Strict quality control was applied to subsequently derive a subset of events to be used for the tomographic inversion (below); the higher quality event subset was comprised of 3570 events.

3. Joint inversion for location and velocity structure

3.1. Inversion approach and model

We jointly solved for *Vp*, *Vp/Vs*, and earthquake hypocentre locations using the double-difference tomography algorithm tomoDDPS (Zhang et al., 2009). This approach allows the combined use of event-pair differential catalogue and waveform-based phase times together with absolute phase data, which allows finer-scale velocity structure to be resolved, as well as relocated event hypocentres (Zhang and Thurber, 2006). Travel times between events and stations are calculated using pseudo-bending raytracing (Um and Thurber, 1987), allowing for variable station elevation and 3-D velocity structure, but assuming a flat earth model. We calculated differential phase times for all pairs of events separated by less than 9 km, in total involving 68731 absolute *P* times, 46001 absolute *S* times, 2285793 differential-phase *P* times, and 1296058 differential-phase *S* times, for 3570 events and 171 stations.

During inversion we varied the relative weighting of absolute phase arrival times and the differential phase times for different iteration steps, following an evolving weighting scheme as described by Zhang and Thurber (2003, 2006). In the initial iteration steps, higher weighting is applied to the absolute phase information, which allows derivation of the larger scale velocity structure. The balance of subsequent weighting is then shifted to the differential phase information in the subsequent iteration steps, allowing derivation of finer-scale velocity structure.

The initial starting 3-D model for inversion for *Vp* and *Vp/Vs* was formed by interpolating the regional model of Eberhart-Phillips et al. (2010) onto a 3-D rectilinear grid, with the Y axis oriented at N39°E, sub-parallel to the (variable) strike of the Taupō Rift (Villamor et al., 2017; Seebeck et al., 2014) (Fig. 1). Progressive inversions were then carried out, starting with the initial model, and slowly decreasing the spacing of the inversion nodes in subsequent inversion runs, following the approach of Eberhart-Phillips and Michael (1993) for inversion stability. Staggered gridding (e.g. Vesnaver and Böhm, 2000 was used at intermediate stages, to test inversion ambiguities and the stability of the response to node positions. In the final model the inversion node spacing was 4 km for nodes close to the axis of the Taupō Rift (Figure S3), with coarser node spacing further away from the rift axis, in areas where the seismic path density was lower (e.g. using a variable node spacing of 10-to-25 km at distances more than 40-km from the *Y*-axis, as shown in Figure S3). The vertical nodes in the final inversion were at −1, 1, 3, 5, 7, 9, 11, 14, and 18 kms depth.

3.2. *Data density and path directionality*

The derivative weighted sum (*DWS*) is a measure of the weighted ray length calculated at each inversion node (Thurber, 1983), providing a relative measure of seismic path density. We calculated *DWS* values during the inversions, and subsequently used the calculated values as an indicator for path coverage. At 5-km and 7-km depth the calculated *DWS* (Figure S4) is highest beneath Wairakei and Rotokawa geothermal fields, and, to the north, the Orakei Korako geothermal system. Some areas to the north-west, as well as to the east and south-east of Wairakei, have lower path coverage. The areas with lower *DWS* are due to reduced density of seismometer coverage to the north-west and south-east, as well as lower levels of background (crustal) seismicity — there are very few crustal earthquakes west and north-west of the central Taupō Rift. The calculated *DWS* values generally drop off for depths greater than 10 km; the majority of earthquakes in the region are shallower than ~8 km, so event-station paths with longer distance (~50 km or greater) are necessary for sampling greater crustal depths.

Biases can also result from path directionality. Following Kissling (1988) we examined the path directionality by calculating ray path density tensors on each inversion node on the 3-D inversion grid (e.g. Figure S5 for 3, 5, 7 and 9 kms depth). The information provided from the ray density tensors complements the information from *DWS*, highlighting where the path directionality is evenly balanced or, in contrast, where the paths are preferentially biased towards certain directions.

3.3. *Synthetic resolution tests*

Synthetic sparse checkerboard tests (following terminology of Rawlinson and Spakman, 2016) were carried out to examine how potential features may be resolved, for our existing seismic inversion station and existing event distribution. In these tests we calculated synthetic travel times for our known earthquake and seismometer locations through synthetic 3-D velocity models, before subsequent inversion of the synthetic travel times. Synthetic checkerboard models with ± 10% velocity perturbations were created using variable block sizes, following a 'sparse' checkerboard pattern. Inversion results (Fig.S6) derived using the synthetic data show reasonable recovery of the perturbed P-wave velocities (*Vp*) where *DWS* is >~100, for the 3-to-7 km depth range, while there was poorer recovery of the synthetic perturbation anomalies for 9+km depth. Recovery of the synthetic *Vp/Vs* perturbations was generally poor; at 3-km depth for example *Vp/Vs* was only recovered in areas in the immediate vicinity of Wairakei and Rotokawa geothermal fields, while recovery was poorer at greater depths (Fig. S7). The limited recovery of the synthetic *Vp/Vs* perturbations reflects the low *DWS* for *Vp/Vs*.

3.4. *Seismicity relocation*

We used the seismic velocity model derived from the tomographic inversion for relocation of the larger earthquake dataset for the same region, comprised of 9149 earthquakes occurring in the 2009–2021 time period. Final event locations were derived using the double-difference algorithm tomoDDPS algorithm (Zhang et al., 2009), using the absolute phase arrival times combined with the event-pair phase-time differential times. We also utilised event-pair waveform-based differential times (e.g. Zhang and Thurber, 2003; Waldhauser and Ellsworth, 2000), which were calculated using cross-correlation of the waveforms, after application of a 1.5 Hz to 12 Hz bandpass filter. Travel-times for the final hypocentre location analysis were calculated using the newly derived 3-D velocity model, which was fixed for this final relocation analysis. Fig. 2 shows the epicentres of the relocated earthquakes; the event distribution is discussed below.

4. Results

4.1. *Inversion results for Vp and Vp/Vs*

In Fig. 3 we show iso-depth slices through the *P*-wave velocity (*Vp*) volume derived from the tomography inversion, for 3, 5, 7 and 9 km depth. Areas are masked light-grey where the *DWS* is less than 100 (where the seismic path coverage is poorer). Epicentres of the relocated seismic events are projected onto the depth slices, only projecting events with depths ± 1 km for each depth slice.

The *Vp* results for 3-km depth (Fig. 3) show *P*-wave velocities less than 4.5 km/s below the central axis of the Taupō rift. The band of low velocity extends northward from Lake Taupō, tracking beneath the surface trace of the known active faults (e.g. Whangamata fault, Ngangiho fault, Puketarata fault), and extending at least up to the Ngakuru graben (Villamor and Berryman, 2001), on the western side of the Paeroa fault (Fig. 3), north-east of Atiamuri geothermal field (Fig. 2).

These low *Vp* velocities likely represent thick layers of rhyolitic pyroclastics, volcaniclastic sediment layers, and andesitic sediments, similar to that found in geothermal drill holes at Wairakei (Rosenberg et al., 2019; Milicich et al., 2021) and Ngā Tamariki geothermal fields (Chambefort et al., 2016). *Vp* is also lower than 4.5 km/s inside the boundary of the inferred Waiora (WA) caldera (Fig. 1). Calculated *DWS* values (Figure S4) are lower to the south of Waiora caldera for depths shallower than 5 km, as there are few earthquakes in this area and seismometer coverage is limited to the east and southeast.

Vp is higher (above 4.8 km/s, darker blue in Fig. 3), between Wairakei and Ngā Tamariki geothermal fields, as well as to the east of Rotokawa field. These higher velocities are representative of the seismic signature of the meta-sedimentary (greywacke) basement in the subsurface. In the geothermal fields the composite basement terrane (described in detail by Mortimer et al., 2023) has been reached at 3.4 km depth at Ngā Tamariki (Chambefort et al., 2016; Milicich et al., 2020), as well as at 1.8–2.5 km depth in some wells at Rotokawa field (Milicich et al., 2020; McNamara et al., 2016; Wallis et al., 2013).

High *Vp/Vs* (> 1.8) is observed at 2 km depth in the vicinity of Wairakei, Rotokawa, and Ngā Tamariki geothermal fields (Fig. 4). Such *Vp/Vs* values are often associated with higher fluid saturation in fractured rock. At 3-km depth, *Vp/Vs* decreases to less than 1.8 for much of the region, with values less than 1.75 for the area between Wairakei, Rotokawa and Ngā Tamariki (Fig. 4).

At 5-km depth (Fig. 3) *Vp* ranges between ~4.9 km/s to 5.7 km/s, with strong ~10% spatial variability. *Vp* is high (> 5.5 km/s) beneath the Wairakei geothermal field, while a band of low *Vp* extends north from Te Mihi (west Wairakei), beneath the known active surface faults, to the Ngakuru graben, west of the Paeroa Fault (Fig. 3). At around this depth a band of seismicity at the south-western end of the Paeroa fault clearly tracks along the eastern side of the low *Vp* block. Low *Vp* is still observed beneath the inferred Waiora (WA) caldera (north of Mt Tauhara), as well as in the vicinity of Rotokawa (Fig. 3).

Vp/Vs at 5-km depth is predominantly less than 1.70, decreasing to 1.65 in the centre of the region (Fig. 4). Similarly low *Vp/Vs* values have been observed for Kaweka terrane basement rocks in southern North Island (Eberhart-Phillips and Reyners, 2012). The low *Vp/Vs* values (corresponding to a Poisson's ratio less than ~0.22) likely reflects high quartz content in the basement terrane beneath our study region; Christensen (1996) found a nearly linear relationship between decreasing SiO_2 content and increasing Poisson's ratio, for rocks with 55 to 75 wt% SiO_2.

Deeper, at 7 km depth (Fig. 3), *Vp* is mostly greater than 5.7 km/s, other than beneath Wairakei geothermal field, and north of the Whakamaru caldera boundary (e.g east of Ohakuri, in the vicinity of Te Kopia) (Fig. 3). An extensive block with high *Vp* (> 5.9 km/s) is observed to the south of Mt.Tauhara (Fig. 3), south and south-east of Wairakei, extending down the eastern shoreline of Lake Taupō.

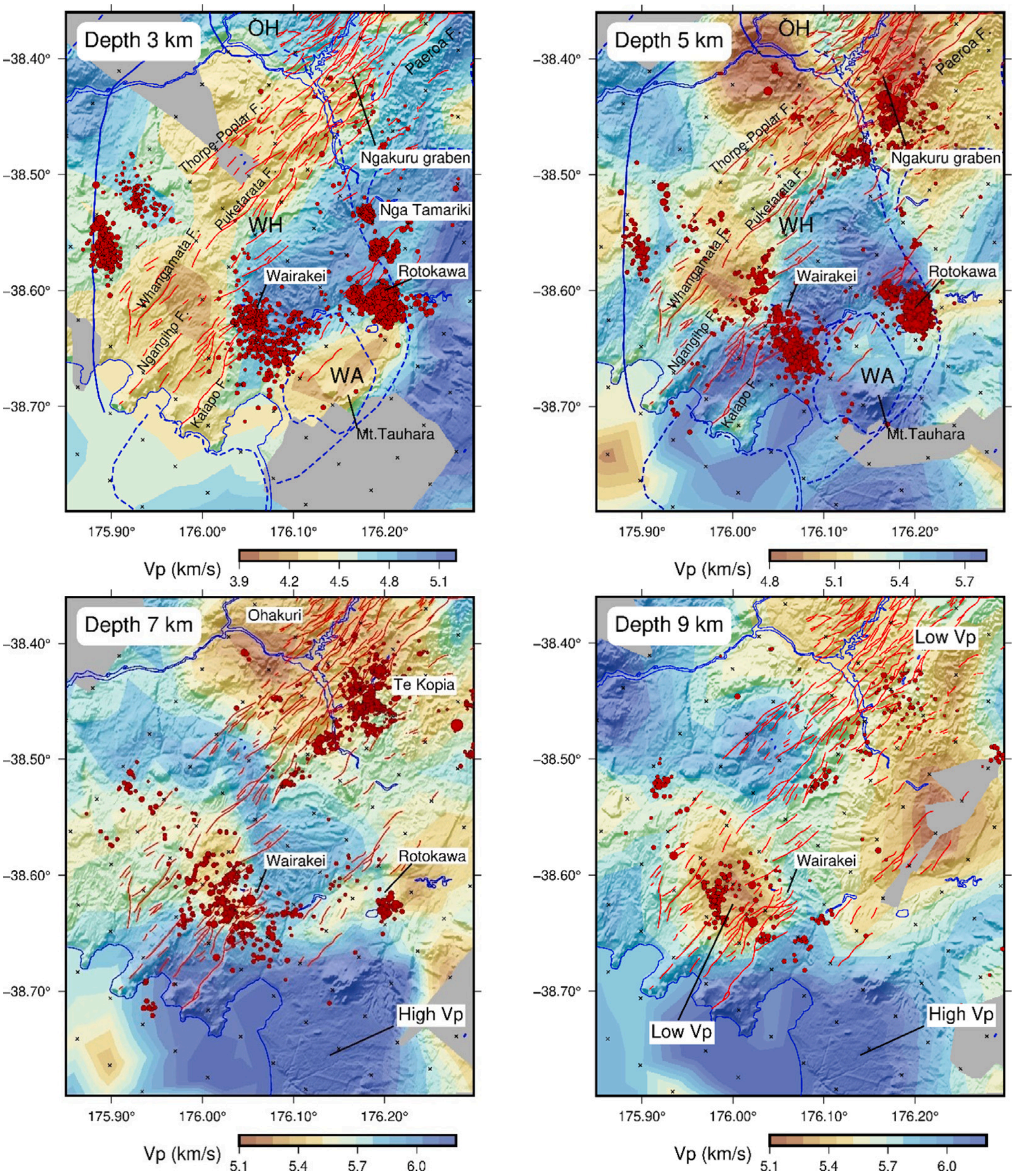

Fig. 3. Derived inversion results for *P*-wave velocity (*Vp*, km/s) at (top left) **3 km** depth, (top-right) **5 km** depth, (bottom-left) **7 km** depth, and (bottom-right) **9 km** depth. Areas with *DWS* values less than 100 are masked grey. Note that the colour scale used is different between the depth slices, to highlight features. Relocated earthquake epicentres are shown (red circles), for events within 1 km of each depth slice. Caldera boundaries for Whakamaru (WH), Ohakuri (OH) and Waiora (WA) are outlined in solid blue lines where surface-expressions are defined, and dashed blue lines where inferred, following Stagpoole et al. (2020), Rosenberg (2017), and Rosenberg (pers.comm). Known active faults from the New Zealand Active Fault database (Langridge et al., 2016), are shown as red segmented lines.

At 9-km depth (Fig. 3) the high *Vp* (> 5.9 km/s) block is still apparent south and south-east of Wairakei, while low *Vp* (< 5.4 km/s) is seen beneath much of the Wairakei area, as well as to the north and north-east of Ngā Tamariki and Rotokawa. The synthetic tests showed reasonable recovery at this depth (Figure S6) north and north-east of Wairakei, while synthetic *Vp* anomalies elsewhere were spatially smeared. The ray density tensors show a reasonable (azimuthally balanced) distribution of path coverage for this depth (Figure S5). *Vp*/*Vs* at this depth is poorly resolved across most of the region — the synthetic reconstruction of *Vp*/*Vs* perturbations is poor and the calculated *DWS* values for *Vp*/*Vs* are low for this depth.

Fig. 5 shows two NW-SE trending cross-sections of *Vp*, along profile-1 and profile-2 (the locations of which are shown in Fig. 2). Profile-1 passes through Rotokawa geothermal field, while profile-2 passes through Wairakei geothermal field and the southern part of the Tauhara field. Three orthogonal cross-sections of *Vp*, each with SW-NE orientation, are shown in Fig. 6, along profile-3, profile-4, and profile-5 (for the profile locations shown in Fig. 2). Profile-3 passes west of Wairakei, extending up to Te Kopia, profile-4 extends from west of Wairakei, through Te Mihi, up to west Ngā Tamariki (Fig. 2), while profile-5 passes between east-Wairakei and Ngā Tamariki (Fig. 2).

On the cross-sections low *Vp* (less than 4 km/s) is observed down to ~2–3 km depth, consistent with the volcaniclastic deposits, fluvial deposits and ignimbrite layers found in the geothermal field drill holes, and consistent with previous regional seismic refraction data (e.g. Stern and Benson, 2011). Higher *Vp* (> 5 km/s) is seen below ~3–4 km depth, although there is considerable (~10%–20%) variation of *Vp* along some of the profiles. On profile-2 (Fig. 5) higher *Vp* (> 6 km/s) is observed to the south-east of Wairakei geothermal field. The high *Vp* (> 6 km/s)

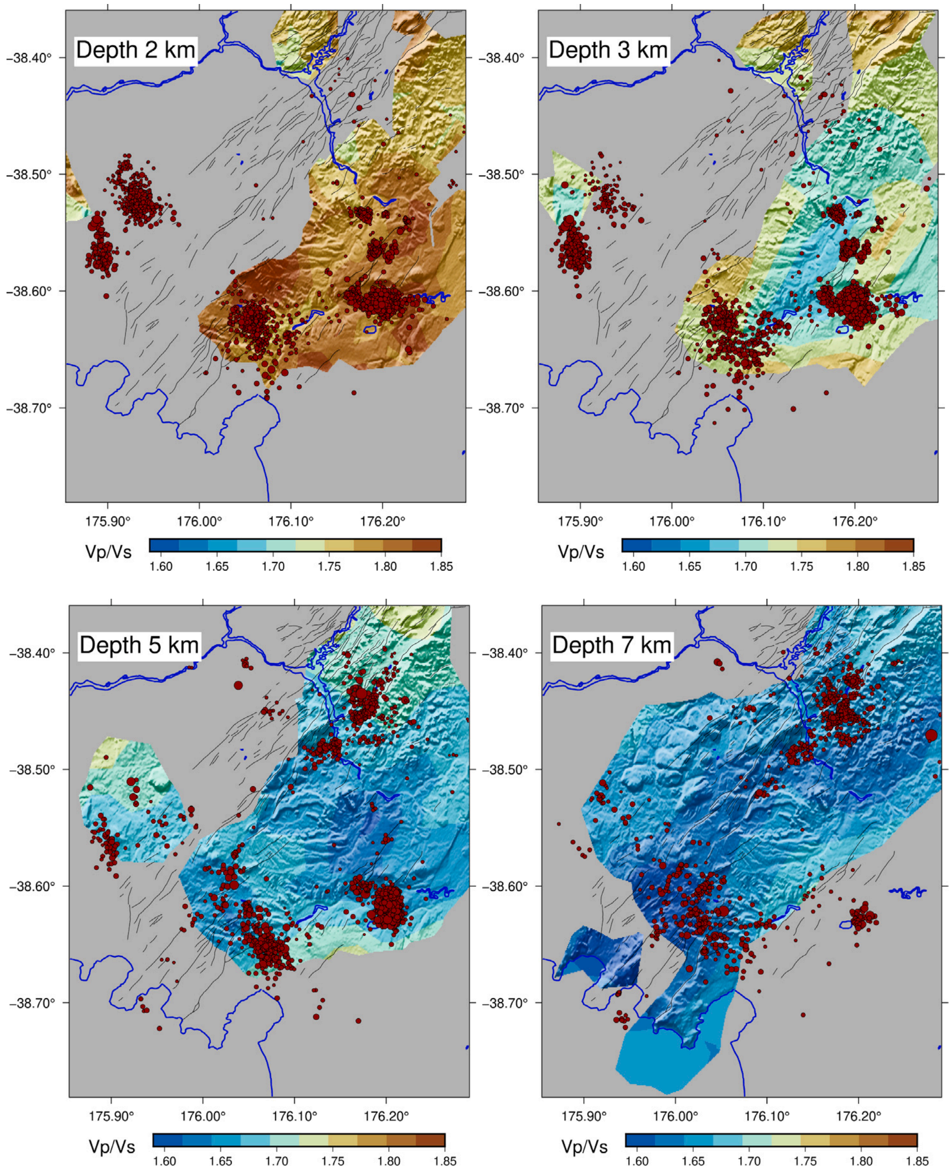

Fig. 4. Derived inversion results for *Vp/Vs* at 2, 3, 5 and 7 km depth. Areas with *DWS-VpVs* values less than 50 are masked grey. Relocated earthquake epicentres are shown (red circles), for events within 1 km of each depth slice.

feature also appears on the SW-NE profiles (e.g. on the SW end of profile-4 and profile-5, labelled as HV1 on Fig. 6).

Low *Vp* anomalies (5.0 km/s to 5.3 km/s) are observed from ~7 to 11 km depth in some areas (Fig. 5; LVL1 and LVL2 in Fig. 6); *Vp* in these anomalies is ~10% lower than in their surroundings. One such *Vp* anomaly lies at ~7–10 kms depth to the north-east of the Ngā Tamariki geothermal field (LVL2 on Profile 5 in Fig. 6), while a separate anomaly lies at ~8 to 11 km depth beneath Wairakei (LVL1 on Profile 4, Profile 5 on Fig. 6).

4.2. Seismicity distribution

Figs. 2 and 3 show the epicentres of more than 9100 earthquakes that we relocated using the new 3-D velocity model. Most of these epicentres show a close spatial association with known geothermal production fields (e.g. Rotokawa, Wairakei, Ngā Tamariki). Seismicity is also observed to the west of Wairakei (‘WW’ in Fig. 2), and near the Te Kopia and Orakei Korako geothermal systems (‘SP’ in Fig. 2), as well as to the north, on the eastern side of the Ngakuru graben (Fig. 1).

Microseismicity previously examined beneath the Wairakei geothermal field (Sepulveda et al., 2015) varies spatially and temporally in the areas used for the geothermal production and fluid reinjection operations. The bulk of this microseismicity is confined to within the shallow boundary of the geothermal field (Sepulveda et al., 2014), although a deeper NW-SE trending feature was noted by Sepulveda et al. (2013) to the west of the field. This deeper seismicity, inferred to indicate pathways for deeper fluid upflow (Sepulveda et al., 2013), is also apparent in our cross-sections (e.g. on Profile 4, X=10–15 km).

In the Rotokawa geothermal field, previous studies have shown that shallow microseismicity mostly occurs in a ~1 km^2 area between fluid re-injection and production zones (Sherburn et al., 2015b). This microseismicity correlates with changes in well flows, pressure and temperature data (Sherburn et al., 2015b; Sewell et al., 2015), with the rate of observed microseismicity closely matching deep fluid re-injection rates (e.g. in early-2010, Sherburn et al., 2015b); pore-pressure changes and poro-elastic stress transfer are thought to also play a role (Hopp et al., 2020). Below 2 km depth event hypocentres correlate to an area of relatively higher resistivity (Heise et al., 2008) matching the highest drilled temperatures in the Rotokawa system

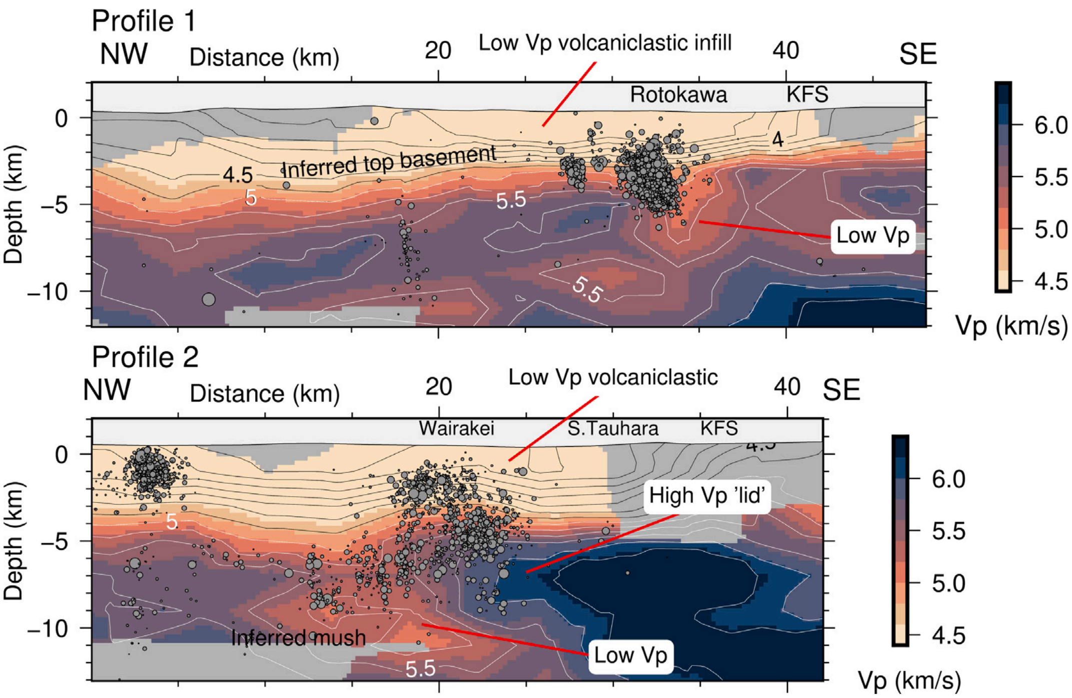

Fig. 5. NW-SE-oriented cross sections of *P*-wave velocity (km/s) along: **(top) profile 1**, passing near Rotokawa geothermal field, and **(bottom) profile 2**, passing near Wairakei field. KFS:Kaingaroa Fault scarp. Velocity contours are shown with 0.25 km/s spacing. Areas with *DWS* values less than 100 are masked with a grey shade. Relocated earthquake hypocentres are projected onto the cross-sections, for events within +/−3 km of the cross-section plane.

(> 250 °C). Heise et al. (2008) inferred that this resistivity signature, and the correlated seismicity, was associated with zones of fracture permeability, feeding high-temperature fluid into the system. Moment tensor solutions derived from regional seismic data by GeoNet (accessed at www.geonet.org.nz) indicate normal faulting mechanisms for larger magnitude ($M_w > 3.3$) events, consistent with NE-SW striking structures (Wallis et al., 2013) inferred from geological data from borehole logging.

The depth distribution of our new relocated hypocentres is shown in Fig. 7 for the Wairakei and Rotokawa geothermal fields. The depth distribution shows that 90% of the Wairakei event depths (termed 'D90') are above 7.1 ± 0.4 km, while 95% of the Wairakei event depths (termed 'D95') are shallower than 7.9 ± 0.5 km, with errors estimated using bootstrap analysis. In contrast, the depth distribution of events in the vicinity of Rotokawa shows that 90% of the Rotokawa events are shallower than 5.1 ± 0.3 km, and 95% shallower than 5.5 ± 0.3 km, ~2 km shallower than for Wairakei. Seismicity cut-off depths are often used as proxies for the depth to the top of the brittle–ductile transition zone (e.g. Ellis et al., 2024; Tryggvason et al., 2002), marking the start of the transition between conditionally-stable brittle (frictional) fault behaviour (above the transition) and aseismic creep behaviour (below the transition) (Ellis et al., 2024). The transition depth and gradient is strongly influenced by temperature and pressure but is also affected by mineralogy, fluid pressure and strain rate (Bürgmann and Dresen, 2008; Ellis et al., 2024).

The relocated seismicity (Fig. 2) shows events south-east of the Paeroa Fault (SP, Fig. 2) on the south-eastern margin of the Ngakuru section of the Taupō Rift (Villamor and Berryman, 2001). These events lie beneath and between the Te Kopia and Orakei Korako geothermal systems (Fig. 2), with most of the hypocentres deeper than 3 km. Surface fault mapping in this area (https://data.gns.cri.nz/af/, last accessed August 2025, Langridge et al., 2016) shows a multitude of rift-fault segments with 20 km length scale (Rowland and Simmons, 2012); such complexity means that the observed seismicity is not easily attributable to any specific surface fault.

5. Discussion

5.1. Near surface layers (0–3+kms)

The depth slice of *Vp* at 3 km depth (Fig. 3) illustrates ~20% spatial heterogeneity of *Vp* across the region, with *Vp* varying from ~4 km/s (west of Wairakei geothermal field) to more than 5.0 km/s (e.g. beneath the Wairakei, Rotokawa and Ngā Tamariki geothermal fields). At shallower depths lower*Vp* velocities of 2.0 to 3.2 km/s have been estimated previously, using 2D seismic refraction data (Harrison and White, 2004; Stern and Benson, 2011). As mentioned, these low velocities are consistent with the known stratigraphy observed in geothermal field drill holes (e.g. Chambefort et al., 2014; Milicich et al., 2021), involving volcaniclastic deposits, fluvial deposits and ignimbrite layers.

Spatially, the *Vp* inversion results for 3-km and 5-km depth (Fig. 3) show a low-*Vp* feature extending from the northern shoreline of Lake Taupō, from around Kaiapo fault, then following northeast beneath the Ngangiho Fault and the Whangamata Fault (labelled on Fig. 3). The low *Vp* feature extends north up to the Ngakuru graben (Fig. 3), where, at 5 km depth, our relocated seismicity is seen to extend along the eastern edge of the low *Vp* feature, close to the southern end of the Paeroa Fault.

This north-east trending low-*Vp* feature follows the dense cluster of known active faults, which mark the surface expression of the Taupō Rift (Fig. 1). The low *Vp* may represent thicker volcaniclastic deposits at 3–5 km depth, possibly linked to crustal extension on the Taupō Rift. Alternatively, *Vp* may be reduced at depth here by the presence of the dense active fault network, with higher fracture density, increased porosity, and the presence of fault gouge (e.g. Mooney and Ginzburg, 1986; Kelly, 2014; Moos and Zoback, 1983). In addition there will also be additional effects on *Vp* from fluid saturation in the faults-fractures (e.g. Mavko et al., 2020).

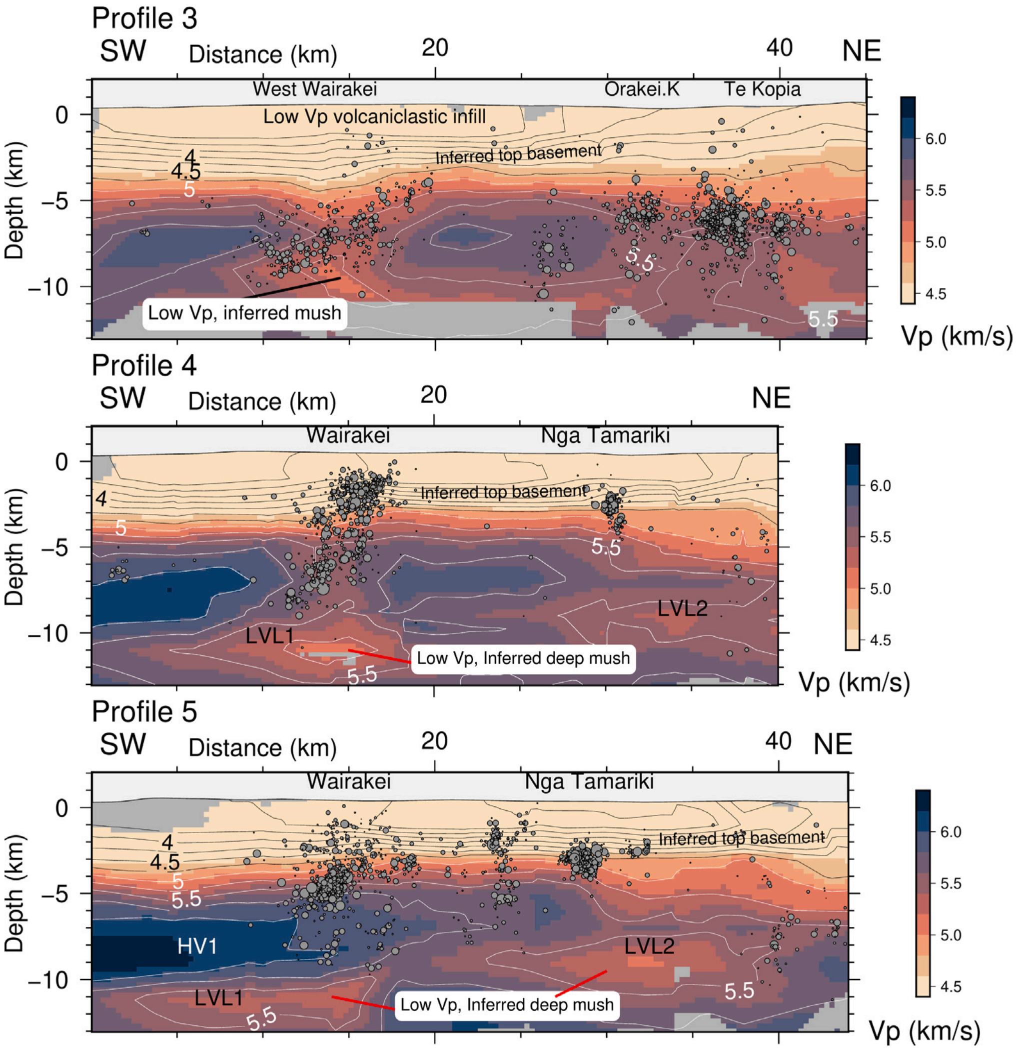

Fig. 6. SW-NE-oriented cross sections of *P*-wave velocity (km/s) along **(top) profile 3** (location shown in Fig. 2), passing west of Wairakei, and through Orakei-Korakei and Te Kopia geothermal systems, **(middle) profile 4**, passing through Te Mihi (west Wairakei geothermal field), and **(bottom) profile 5**, passing between the Wairakei and Ngā Tamariki geothermal fields. LVL1 and LVL2 indicate low velocity anomalies, HV1 indicates a high velocity body. Velocity contours shown with 0.25 km/s spacing. Relocated earthquake hypocentres are projected onto the cross-sections, for events within +/−3 km of each cross-section plane. Focused seismicity is seen beneath Wairakei, from 1 to 8 kms depth, as well as beneath Ngā Tamariki, Orakei Korako and Te Kopia.

5.2. Basement heterogeneity

Higher *Vp* (between 5 and 5.7 km/s) is observed at 3–5 km depth north of Wairakei and west of Rotokawa (Fig. 3), extending north up to Orakei Korako. The higher *Vp* most likely represents the Mesozoic metasedimentary (greywacke) basement; a similar range of *Vp* is found for laboratory measurements of greywacke basement rocks from this region (e.g. McNamara et al., 2014; Mielke et al., 2016; Melia et al., 2022). Greywacke basement has been encountered in some of the geothermal wells at Ngā Tamariki (3.4 km depth, Chambefort et al., 2016), Rotokawa field (1.8–2.8 km depth, Milicich et al., 2020; McNamara et al., 2016) as well as at Ohaaki field (1.6 km depth, Milicich et al., 2020), although not in boreholes at the Wairakei field.

Other than the greywacke meta-sedimentary terranes, it is also likely that cooled sills and plutons are present in the mid-upper crust, given the extensive volcanism in the study region (e.g. Chambefort et al., 2014, 2016; Chambefort and Dilles, 2023; Harmon et al., 2024a,b). The expected range of *Vp* for the greywacke basement terranes (e.g. Melia, 2016; Melia et al., 2022; Christensen and Okaya, 2007) overlaps that expected for intermediate to silicic plutons (e.g. Christensen, 1979), depending on the exact mineral composition. This expected overlap makes it difficult to distinguish the rock type on the basis of *Vp* alone, as noted by Mortimer et al. (2023) and Milicich et al. (2020).

The *Vp/Vs* results from the inversion (Fig. 4) suggest *Vp/Vs* values less than 1.65 for depths greater than ~3 km. Such low *Vp/Vs* values would be consistent with greywacke terrane with a high quartz content, such as the Torlesse Composite Terrane metasedimentary rocks (Mortimer et al., 2023), but would also be consistent with high SiO_2 granite.

Below ~5 km depth the cross-sections of *Vp* (Figs. 5 and 6) show lateral heterogeneity, with ~10%–20% changes in *Vp* over spatial distances of 10 km. Profile 2 (Fig. 5) for example shows a high-*Vp* ‘lid’ with *Vp* > 5.5 km/s at ~5–7 km depth, while just to the northwest *Vp* decreases to ~5 km/s. Seismicity in the same location and depth range is notably elevated at 5 to 8 kms depth on profile 2 (Fig. 5) as well as on profiles 3 and 4, below and west of Wairakei (Fig. 6).

5.3. Mid-crustal low-Vp anomalies: magmatic mush ?

Below 5–7 km depth we observe several low *Vp* anomalies with *Vp* less than 5.5 km/s, ~10% lower than the surroundings (Fig. 3). A clear example is at ~8–11 km depth beneath Wairakei geothermal field (Fig. 5 profile 2, X=20 km and X=15; ‘labelled LVL1’ on profiles 3 and 4 in

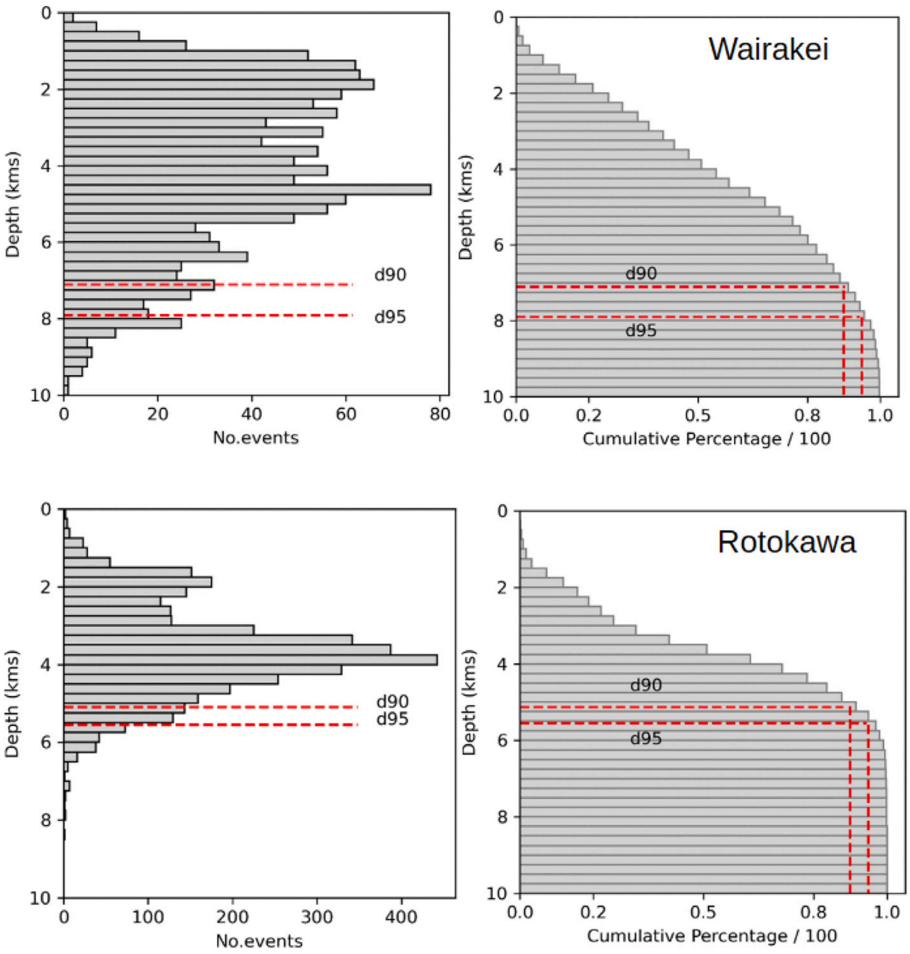

Fig. 7. **Top row :** Depth histogram (top-left), and Cumulative histogram (top-right) for earthquakes near Wairakei (area shown in Fig. 2). 90% of the Wairakei events ("D90") are shallower than 7.1 (± 0.4) km, and 95% of the events ("D95") are shallower than 7.9 (± 0.5) km. **Bottom row :** Depth histogram (bottom-left) and cumulative histogram (bottom-right) for earthquakes near Rotokawa (area shown in Fig. 2). 90% of the Rotokawa events are shallower than 5.1 (± 0.2) km, and 95% of the events are shallower than 5.5 (± 0.3) km. Error bounds derived using bootstrap sampling.

Fig. 6), while there is a slightly shallower anomaly (~7–10 km) beneath and north of Ngā Tamariki (labelled 'LVL2' on X=30–35 km on profiles 4 and 5), as well as at ~5–8 km depth near Rotokawa (X=35 km on Profile 1, Fig. 5).

Changes in *Vp* can result from rock composition, fluid content, fractures, and thermal effects, amongst other factors; unique interpretation is not feasible without cross-comparison with other geophysical observations (e.g. *Vp/Vs*, *Vs*, seismic attenuation, electrical conductivity, gravity). If *Vp/Vs* was resolvable then it would help constrain the interpretation, as it is sensitive to rock composition, the presence of partial melt, the presence of cracks, and the degree of pore fluid saturation. Unfortunately, *Vp/Vs* is only well resolved down to ~5 km depth with our current data.

Partial melt with less than ~4% melt fraction has previously been inferred to lie below this region. Inversion of rift-scale magnetotelluric (MT) data acquired across the TVZ shows a sharp increase in conductivity at 10 km depth (Heise et al., 2007), inferred to represent interconnected melt fraction (<~4%; (Heise et al., 2007)). More recently, with data from extensive MT arrays, with sites spaced 2 km apart, shallower localised zones of low resistivity (< 30 Ω-m) have been imaged at 3–7 km depth in the vicinity of Rotokawa, Ohaaki and Ngā Tamariki geothermal systems (Fig. 2) (Bertrand et al., 2012, 2015); these localised zones are inferred to represent partial melt and/or interconnected saline fluid (Bertrand et al., 2015). The resistivity models of the 2-km-spaced array MT data resolve heterogeneity in the mid-crust, with broad zones of increased conductivity occurring at ~8 km depth, interpreted to mark the top of the underlying magmatic systems driving heat through the overlying brittle crust (e.g. Bertrand et al., 2022).

Matching the conductivity interpretation, we interpret the observed low-*Vp* anomalies to represent bodies of crystal-rich magma mush in the mid-crust, with a low percentage of interstitial melt. *Vp* is expected to decrease if there is even a small percentage of interstitial melt present (Paulatto et al., 2019, 2022), in part due to temperature effects linked to the solid-melt phase transition (Lyakhovsky et al., 2021). The extent of any changes in *Vp* would depend on the microscopic distribution of the melt, melt dimensions and melt fraction, as well as on the presence of volatile bubbles in the melt (Paulatto et al., 2019). In addition, *Vp* would also be affected by any magmatically-derived saline fluids, as well as by the fracture density in rock above the melt.

Interpreting the low-*Vp* anomalies e.g. 'LVL1' and 'LVL2' (Fig. 6) as near-solidus magma mush bodies, there appears to be at least two spatially-separated mid-lower crust bodies immediately apparent — the first beneath Wairakei geothermal field at ~8–11 km depth ('LVL1' on profiles 4 and 5, Fig. 6), and a second slightly shallower at ~7–10 km depth beneath, and to the north of, Ngā Tamariki geothermal field ('LVL2' on Fig. 6). A separate shallower anomaly is also imaged at ~5–8 km depth beneath Rotokawa geothermal field (profile 1, Fig. 5).

It is difficult to reconcile the composition of magma mush at these depths unequivocally, due to the lack of a clear connection between moderately high conductivity, low-*Vp* and geochemistry. However, the relatively deep anomalies down at ~10 km are more likely to represent mafic to intermediate magma reservoirs, whereas shallower anomalies

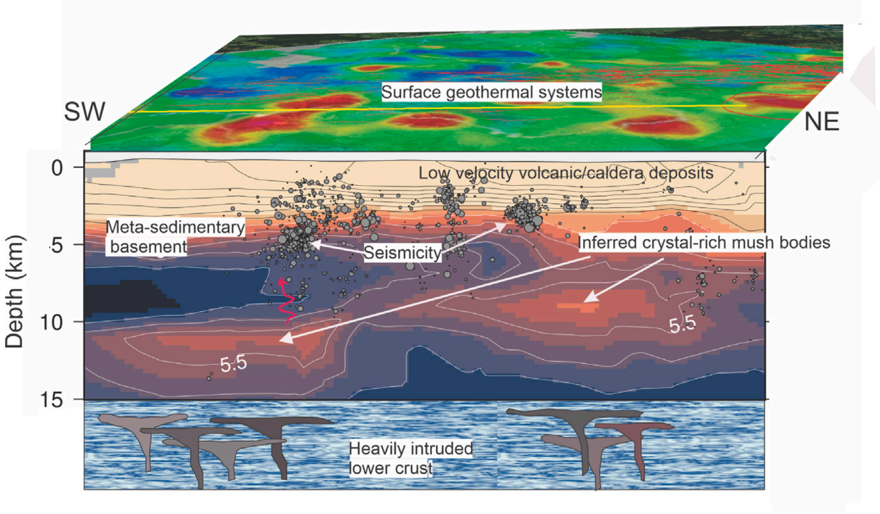

Fig. 8. Conceptual schematic of the mid-crustal structure beneath the study region.

are likely rhyolitic in composition. These shallow anomalies may represent the remnants of past explosive eruptions in this volcanically active region.

Similar mid-crustal low *Vp* values observed elsewhere in other volcanic settings are often attributed to the effect of partial melt and magmatic systems, although *Vp/Vs* is required to constrain any interpretation (Lin, 2015). Below Mt.St.Helens, Ulberg et al. (2020) observed a ~3%–6% *Vp* reduction in the mid-crust at 6–15 km depth, which they interpreted as a signature of partial melt. Similarly a low *Vp* anomaly observed at 4.2–6.2 km depth beneath Long Valley caldera (Lin, 2015) was inferred to represent partial melt, as was a 10% reduction in *Vp* beneath Yellowstone caldera at 5-to-16 km depth (Huang et al., 2015), following similar interpretations by Husen et al. (2004).

Fig. 8 shows a schematic of our conceptual interpretation. Low velocity volcaniclastic deposits extend down to ~2–3 km depth, overlying metasedimentary basement. The basement, as imaged by *Vp* (darkest blue), varies considerably across the region, likely altered by caldera volcanism. Observed seismicity includes earthquake clusters beneath the known geothermal systems (e.g. Wairakei, Rotokawa, Ngā Tamariki), while fault-fracture networks associated with the seismicity at 5–8 kms (e.g. west of Wairakei geothermal field) mark the permeability pathways that can promote the upward migration of volatiles from the brittle–ductile transition. In the mid-lower crust, we interpret several distinct, spatially separated, magma mush bodies, likely with a small percentage of interstitial melt.

6. Conclusions

We have examined the seismicity distribution and velocity structure in the central part of the TVZ, using seismic data recorded by temporary campaign and permanent network seismometers. We find :

- Derived P-wave velocity (*Vp*) indicates that the mid-crust beneath the region varies considerably across the region, with spatial variations in the order of ~10–20% over distance scales of ~10 km, especially at 5-to-11 km depth. This crustal heterogeneity may reflect the extensive past volcanic activity in the region, and the possible presence of volcanic sills and granite bodies in the basement.
- Observed seismicity includes clusters of activity beneath the known geothermal systems (e.g. Wairakei, Rotokawa, Ngā Tamariki), but also includes deeper events west of Wairakei field and the Paeroa fault. This seismicity highlights the location of fault networks in the basement (especially beneath Wairakei) - permeability pathways which can promote the migration of volatiles. The depth distribution of the highest-quality hypocentres shows that 90% of the seismicity ('D90') beneath Wairakei is shallower than 7.1 +/−0.4 km, while the same 90% cut-off for seismicity below Rotokawa is shallower, at 5.1 +/−0.3 km; these are measures of the seismicity depth cut-off, indicative of the top of the brittle–ductile transition, varying spatially.
- In the mid-lower crust (5–11 km) we image several distinct separated bodies with relatively low *Vp* values (< 5.5 km/s), which we infer to represent deep-seated crystal-rich magma mush with a low percentage of melt. The most distinct of these bodies lies beneath and west of Wairakei geothermal field, while a second body lies beneath and north of Ngā Tamariki field, extending beneath Orakei Korako and Te Kopia geothermal systems.

Currently, our interpretation of the low-*Vp* anomalies is not unique; additional observations of other geophysical properties are needed for improved constraint, such as body-wave seismic attenuation (*Qp*, *Qs*) and improved *Vs* and *Vp/Vs* estimates. Seismic attenuation, for example, is sensitive to temperature and partial melt (Jaya et al., 2010; Sanders et al., 1995), while additional shear wave information (derivable for example from ambient seismic noise studies) would help to constrain *Vs*, and *Vp/Vs*. Future joint interpretation of seismic properties together with electrical conductivity derived from magnetotelluric studies (e.g. Heise et al., 2008; Bertrand et al., 2012, 2015) is also expected to be informative.

CRediT authorship contribution statement

Stephen Bannister: Writing – review & editing, Writing – original draft, Methodology, Investigation. **Edward A. Bertrand:** Writing – review & editing, Writing – original draft, Validation, Project administration. **Geoff Kilgour:** Writing – review & editing, Writing – original draft. **T. Grant Caldwell:** Writing – review & editing, Writing – original draft. **Isabelle Chambefort:** Writing – review & editing, Writing – original draft, Project administration, Funding acquisition, Conceptualization. **Wiebke Heise:** Writing – review & editing, Writing – original draft. **Sandra Bourguignon:** Writing – review & editing, Writing – original draft, Investigation, Data curation.

Declaration of competing interest

The authors declare that they have no known competing financial interests or personal relationships that could have appeared to influence the work reported in this paper.

Acknowledgements

We thank GNS Science Wairakei staff for their field support in seismic array deployments carried out in 2009–2011. National seismometer data were provided by GeoNet (https://www.geonet.org.nz), which is sponsored by the New Zealand government through its agencies Earthquake Commission (EQC), GNS Science, and Land Information New Zealand. Thanks to Contact Energy and Mercury NZ for access to their seismological data, and to Haijiang Zhang for use of his *tomoDD* code. Thanks to two anonymous reviewers, who made useful suggestions for improving the manuscript. Analysis of seismic data was facilitated using *Obspy* (Beyreuther et al., 2010); maps and plots were created using *Matplotlib* (Hunter, 2007) and *PyGMT* (Uieda et al., 2021). This research was carried out under the Geothermal: The Next Generation research programme, funded by the New Zealand Ministry of Business, Innovation and Employment (MBIE contract C05X1904). The work was also supported by MBIE, New Zealand through the Understanding Zealandia/Te Riu-a-Maui research programme.

Appendix A. Supplementary data

Supplementary material related to this article can be found online at https://doi.org/10.1016/j.jvolgeores.2025.108448.

Data availability

GeoNet continuous seismic waveform data, seismometer metadata and moment tensor solutions are openly available through the GeoNet website (http://www.geonet.org.nz). Seismic waveform data, as well as seismometer metadata, are also available using FDSN services from IRIS-DMC. Waveform data from the temporary HADES (2009–2011) seismometers are also available from the IRIS-DMC data management centre, under network code Z8 (Bannister, 2009). The catalog of earthquake relocations is available on https://github.com/nephets-b/2025_seismic_imaging.

References

Bannister, S., 2009. Deep geothermal HADES seismic array. http://dx.doi.org/10.7914/SN/Z8_2009.

Barker, S.J., Rowe, M.C., Wilson, C.J.N., Gamble, J.A., Rooyakkers, S.M., Wysoczanski, R.J., Illsley-Kemp, F., Kenworthy, C.C., 2020. What lies beneath? reconstructing the primitive magmas fueling voluminous silicic volcanism using olivine-hosted melt inclusions. Geology 48, 504–508. http://dx.doi.org/10.1130/G47422.1.

Bégué, F., Guilda, G., Ghiorso, M., Pamukcu, A., Kennedy, B., Gravley, D., Deering, C., Chambefort, I., 2014. Phase-equilibrium geobarometers for silicic rocks based on rhyolite-MELTS. Part 2: application to Taupo Volcanic Zone rhyolites. Contrib. Miner. Pet. 168, 1082. http://dx.doi.org/10.1007/S00410-014-1082-7.

Bertrand, E.A., Caldwell, T.G., Bannister, S., Soengkono, S., Bennie, S.L., Hill, G.J., Heise, W., 2015. Using array MT data to image the crustal resistivity structure of the southeastern Taupo Volcanic Zone, New Zealand. J. Volcanol. Geotherm. Res. 305, 63–75. http://dx.doi.org/10.1016/j.jvolgeores.2015.09.020.

Bertrand, E.A., Caldwell, T.G., Hill, G.J., Wallin, E.L., Bennie, S.L., Cozens, N., Onacha, S.A., Ryan, G.A., Walter, C., Zaino, A., Wameyo, P., 2012. Magnetotelluric imaging of uppercrustal convection plumes beneath the Taupo Volcanic Zone, New Zealand. Geophys. Res. Lett. 39, http://dx.doi.org/10.1029/2011gl050177.

Bertrand, E., Kannberg, P., Caldwell, T., Heise, W., Constable, S., Scott, B., Bannister, S., Kilgour, G., Bennie, S., Hart, R., Palmer, N., 2022. Inferring the magmatic roots of volcano-geothermal systems in the Rotorua caldera and Okataina Volcanic Centre from magnetotelluric models. J. Volcanol. Geotherm. Res. 431, http://dx.doi.org/10.1016/j.jvolgeores.2022.107645.

Beyreuther, M., Barsch, R., Krischer, L., Megies, T., Behr, Y., Wassermann, J., 2010. Obspy: A python toolbox for seismology. Seismol. Res. Lett. 81, 530–533.

Bibby, H., Caldwell, T., Davey, F., Webb, T., 1995. Geophysical evidence on the structure of the taupo volcanic zone and its hydrothermal circulation. J. Volcanol. Geotherm. Res. 68, 29–58.

Bindeman, I., 2024. Reinterpretation of the post-26 ka Taup rhyolitic magmatic system (New Zealand) as deep and vertically extensive based on isotope thermometry and measured and modeled zircon destinies. J. Petrol. 65.

Browne, P., Graham, I., Parker, R., Wood, C., 1992. Subsurface andesite lavas and plutonic rocks in the Rotokawa and Ngatamariki geothermal systems, Taupo volcanic zone, New Zealand. J. Volcanol. Geotherm. Res. 51, 199–215.

Bryan, C.J., Sherburn, S., Bibby, H.M., Bannister, S.C., Hurst, A.W., 1999. Shallow seismicity of the central Taupo Volcanic Zone, New Zealand: Its distribution and nature. N. Z. J. Geol. Geophys. 42, 533–542. http://dx.doi.org/10.1080/00288306.1999.9514859.

Bürgmann, R., Dresen, G., 2008. Rheology of the lower crust and upper mantle: Evidence from rock mechanics, geodesy, and field observations. Annu. Rev. Earth Planet. Sci 36, 531–567.

Chambefort, I., Buscarlet, E., Wallis, I.C., Sewell, S., Wilmarth, M., 2016. Ngatamariki Geothermal Field, New Zealand: Geology, geophysics, chemistry and conceptual model. Geothermics 59, 266–280. http://dx.doi.org/10.1016/j.geothermics.2015.07.011.

Chambefort, I., Dilles, J.H., 2023. Chemical vectoring in continental geothermal systems: Composition of altered rocks and illite as guides to magmatic degassing. Geothermics 110, http://dx.doi.org/10.1016/j.geothermics.2023.102682.

Chambefort, I., Lewis, B., Wilson, C., Rae, A., Coutts, C., Bignall, G., Ireland, T., 2014. Stratigraphy and structure of the Ngatamariki geothermal system from new zircon UPb geochronology: Implications for Taupo Volcanic Zone evolution. J. Volcanol. Geotherm. Res. 274, 1–20. http://dx.doi.org/10.1016/j.jvolgeores.2014.01.015.

Christensen, N.I., 1979. Compressional wave velocities in rocks at high temperatures and pressures, critical thermal gradients, and crustal low-velocity zones. J. Geophys. Res.: Solid Earth 84, 6849–6857.

Christensen, N.I., 1996. Poisson's ratio and crustal seismology. Journal of geophysical research. Solid Earth 101, 3139–3156. http://dx.doi.org/10.1029/95jb03446.

Christensen, N.I., Okaya, D.A., 2007. Compressional and shear wave velocities in South Island, New Zealand rocks and their application to the interpretation of seismological models of the New Zealand crust. Geophys. Monogr. Ser. 175, 123–155. http://dx.doi.org/10.1029/175GM08.

Cole, J.W., Spinks, K.D., 2009. Caldera volcanism and rift structure in the Taupo Volcanic Zone, New Zealand. Geol. Soc. Lond. Spec. Publ. 327, 9–29. http://dx.doi.org/10.1144/sp327.2.

Eberhart-Phillips, D., Bannister, S., Reyners, M., Henrys, S., 2020. New Zealand wide model 2.2 seismic velocity and Qs and Qp models for New Zealand. http://dx.doi.org/10.5281/zenodo.3779523.

Eberhart-Phillips, D., Michael, A.J., 1993. Three-dimensional velocity structure, seismicity, and fault structure in the Parkfield region, central California. J. Geophys. Res.: Solid Earth 98, 15737–15758.

Eberhart-Phillips, D., Reyners, M., 2012. Imaging the Hikurangi Plate interface region, with improved local-earthquake tomography. Geophys. J. Int. 190, 1221–1242.

Eberhart-Phillips, D., Reyners, M., Bannister, S., Chadwick, M., Ellis, S., 2010. Establishing a versatile 3-D seismic velocity model for New Zealand. Seismol. Res. Lett. 81, 992–1000.

Ellis, S., Bannister, S., Dissen, R.Van., Eberhart-Phillips, D., Boulton, C., Reyners, M., Funnell, R., Mortimer, N., Upton, P., Rollins, C., Seebeck, H., 2024. New Zealand fault-rupture depth model v.1.0: A provisional estimate of the maximum depth of seismic rupture on New Zealands active faults. Bull. Seismol. Soc. Am. http://dx.doi.org/10.1785/0120230166.

Gale, N., Gledhill, K., Chadwick, M., Wallace, L., 2015. The Hikurangi margin continuous GNSS and seismograph network of New Zealand. Seismol. Res. Lett. 86, 101–108.

Gamble, J., Smith, I., McCulloch, M., Graham, I., Kokelaar, B., 1993. The geochemistry and petrogenesis of basalts from the Taupo Volcanic Zone and Kermadec Island Arc, SW Pacific. J. Volcanol. Geotherm. Res. 54, 265–290.

Harmon, L.J., Gualda, G.A.R., Gravley, D.M., Smithies, S., Deering, C., 2024a. The Whakamaru magmatic system (Taupo Volcanic Zone, NewZealand), Part 1: Evidence from Tephra deposits the multipl magma types through times. J. Volcanology Geotherm Res 445.

Harmon, L.J., Smithies, S.L., Gualda, G.A.R., Gravley, D.M., 2024b. The Whakamaru magmatic system (Taup Volcanic Zone, New Zealand), part 2: Evidence from ignimbrite deposits for the pre-eruptive distribution of melt-dominated magma and magma mush. J. Volcanol. Geotherm. Res. 447, http://dx.doi.org/10.1016/j.jvolgeores.2024.108013.

Harrison, A.J., White, R.S., 2004. Crustal structure of the Taupo Volcanic Zone, New Zealand: Stretching and igneous intrusion. Geophys. Res. Lett. 31, 2–5. http://dx.doi.org/10.1029/2004GL019885.

Harrison, A., White, R.S., 2006. Lithospheric structure of an active backarc basin: the Taupo Volcanic Zone, New Zealand. Geophys. J. Int. 167, 968–990. http://dx.doi.org/10.1111/j.1365-246X.2006.03166.x.

Heise, W., Bibby, H.M., Caldwell, T.G., Bannister, S.C., Ogawa, Y., Takakura, S., Uchida, T., 2007. Melt distribution beneath a young continental rift: The Taupo Volcanic Zone, New Zealand. Geophys. Res. Lett. 34, http://dx.doi.org/10.1029/2007gl029629.

Heise, W., Caldwell, T.G., Bibby, H.M., Bannister, S.C., 2008. Three-dimensional modelling of magnetotelluric data from the Rotokawa geothermal field, Taupo Volcanic Zone, New Zealand. Geophys. J. Int. 173, 740–750. http://dx.doi.org/10.1111/j.1365-246X.2008.03737.x.

Heise, W., Caldwell, T.G., Bibby, H.M., Bennie, S.L., 2010. Three-dimensional electrical resistivity image of magma beneath an active continental rift, Taupo Volcanic Zone, New Zealand. Geophys. Res. Lett. 37, http://dx.doi.org/10.1029/2010gl043110.

Hopp, C., Sewell, S., Mroczek, S., Savage, M., Townend, J., 2020. Seismic response to evolving injection at the Rotokawa geothermal field, New Zealand. Geothermics 85, http://dx.doi.org/10.1016/j.geothermics.2019.101750.

Huang, H.H., Lin, F.C., Schmandt, B., Farrell, J., Smith, R.B., Tsai, V.C., 2015. The Yellowstone magmatic system from the mantle plume to the upper crust. Science 348.

Hunter, J.D., 2007. Matplotlib: A 2d graphics environment. Comput. Sci. Eng. 9, http://dx.doi.org/10.1109/MCSE.2007.55.

Husen, S., Hardebeck, J., 2010. Understanding seismicity catalogs and their problems. Community Online Resour. Stat. Seism. Anal..

Husen, S., Smith, R.B., Waite, G.P., 2004. Evidence for gas and magmatic sources beneath the Yellowstone volcanic field from seismic tomographic imaging. J. Volcanol. Geotherm. Res. 131, 397–410. http://dx.doi.org/10.1016/S0377-0273(03)00416-5.

Imperatori, W., Mai, P.M., 2015. The role of topography and lateral velocity heterogeneities on near-source scattering and ground-motion variability. Geophys. J. Int. 202, 2163–2181.

Jaya, M.S., Shapiro, S.A., Kristinsdóttir, L.H., Bruhn, D., Milsch, H., Spangenberg, E., 2010. Temperature dependence of seismic properties in geothermal rocks at reservoir conditions. Geothermics 39, 115–123. http://dx.doi.org/10.1016/j.geothermics.2009.12.002.

Kelly, C., 2014. Understanding Seismic Properties of Fault Zones. (Ph.D. thesis). University of Liverpool.

Kissling, E., 1988. Geotomography with local earthquake data. Rev. Geophys. 26, 659–698.

Langridge, R., Ries, W., Litchfield, N., Villamor, P., Dissen, R.Van., Barrell, D., Rattenbury, M., Heron, D., Haubrock, S., Townsend, D., 2016. The New Zealand active faults database. N. Z. J. Geol. Geophys. 59, 86–96.

Lin, G., 2015. Seismic velocity structure and earthquake relocation for the magmatic system beneath Long Valley Caldera, eastern California. J. Volcanol. Geotherm. Res. 296, 19–30. http://dx.doi.org/10.1016/j.jvolgeores.2015.03.007.

Lomax, A., 2005. A reanalysis of the hypocentral location and related observations for the great 1906 California earthquake. Bull. Seismol. Soc. Am. 95, 861–877. http://dx.doi.org/10.1785/0120040141.

Lomax, A., Michelini, A., Curtis, A., 2007. Earthquake Location, Direct, Global-Search Methods. Springer.

Lomax, A., Virieux, J., Volant, P., Berge, C., 2000. Probabilistic earthquake location in 3D and layered models: Introduction of a Metropolis-Gibbs method and comparison with linear locations. In: Advances in Seismic Event Location. Kluwer, pp. 101–134.

Lyakhovsky, V., Shalev, E., Kurzon, I., Zhu, W., Montesi, L., Shapiro, N.M., 2021. Effective seismic wave velocities and attenuation in partially molten rocks. Earth Planet. Sci. Lett. 572, 117117. http://dx.doi.org/10.1016/j.epsl.2021.117117.

Mauriohooho, K., 2023. Geochronology and Geochemical Evolution of Magma Systems in the Taup-Maroa Area Between Two Supereruptions: Whakamaru and Ruanui Doctoral dissertation. Te Herenga Waka-Victoria University of Wellington.

Mavko, G., Mukerji, T., Dvorkin, J., 2020. Fluid effects on wave propagation. In: The Rock Physics Handbook, Chapter 6. Cambridge University press., pp. 367–473.

McNamara, D.D., Faulkner, D., McCarney, E., 2014. Rock properties of greywacke basement hosting geothermal reservoirs, New Zealand: Preliminary results. In: 39th Workshop on Geothermal Reservoir Engineering. http://dx.doi.org/10.13140/RG.2.1.1304.2160.

McNamara, D.D., Sewell, S., Buscarlet, E., Wallis, I.C., 2016. A review of the Rotokawa geothermal field, New Zealand. Geothermics 59, 281–293.

Melia, A., 2016. Characterisation of the Greywacke Basement of Taupo Volcanic Zone Geothermal Fields, New Zealand. (Ph.D. thesis). University of Liverpool.

Melia, A., Faulkner, D.R., McNamara, D.D., 2022. Physical property characterization of the Waipapa greywacke: an important geothermal reservoir basement rock in New Zealand. Geotherm. Energy 10, http://dx.doi.org/10.1186/s40517-022-00218-2, 11–11.

Mielke, P., Weinert, S., Bignall, G., Sass, I., 2016. Thermo-physical rock properties of greywacke basement rock and intrusive lavas from the Taupo Volcanic Zone, New Zealand. J. Volcanol. Geotherm. Res. 324, 179–189. http://dx.doi.org/10.1016/j.jvolgeores.2016.06.002.

Milicich, S.D., Chambefort, I., Simpson, M.P., Wilson, C.J.N., Alcarez, S., Calibugan, A., Bardsley, C., Morales, A.G., 2021. Geology, geochronology, alteration and geochemistry of the rotokawa geothermal system, taupo volcanic zone, New Zealand. In: World Geothermal Congress 2020+1, Reykjavik, Iceland. pp. 1–12.

Milicich, S.D., Mortimer, N., Villamor, P., Wilson, C.J.N., Chambefort, I., Sagar, M.W., Ireland, .T.R., 2020. The Mesozoic terrane boundary beneath the Taupo Volcanic Zone, New Zealand, and potential controls on geothermal system characteristics. N. Z. J. Geol. Geophys. 1–12. http://dx.doi.org/10.1080/00288306.2020.1823434.

Mooney, W.D., Ginzburg, A., 1986. Seismic measurements of the internal properties of fault zones. Pure Appl. Geophys. 124, 141–157.

Moos, D., Zoback, M.D., 1983. In situ studies of velocity in fractured crystalline rocks. J. Geophys. Res.: Solid Earth 88, 2345–2358.

Mortimer, N., Charlier, B.L.A., Rooyakkers, S.M., Turnbull, R.E., Wilson, C.J.N., Negrini, M., Bannister, S., Milicich, S.D., Chambefort, I., Miller, C.A., Kilgour, G., 2023. Crustal basement terranes under the Taup Volcanic Zone, New Zealand: Context for hydrothermal and magmatic processes. J. Volcanol. Geotherm. Res. http://dx.doi.org/10.1016/j.jvolgeores.2023.107855.

Mousavi, S.M., Ellsworth, W.L., Zhu, W., Chuang, L.Y., Beroza, G.C., 2020. Earthquake transformeran attentive deep-learning model for simultaneous earthquake detection and phase picking. Nat. Commun. 11, 1–12.

Okamoto, K., Mukuhira, Y., Darisma, D., Asanuma, H., Moriya, H., 2024. Machine learning automatic picker for geothermal microseismicity analysis for practical purposes to reveal fine reservoir structures. Geothermics 116, http://dx.doi.org/10.1016/j.geothermics.2023.102832.

Paulatto, M., Hooft, E.E.E., Chrapkiewicz, K., Heath, B., Toomey, D.R., Morgan, J.V., 2022. Advances in seismic imaging of magma and crystal mush. Front. Earth Sci. 10.

Paulatto, M., Moorkamp, M., Hautmann, S., Hooft, E., Morgan, J.V., Sparks, R.S.J., 2019. Vertically extensive magma reservoir revealed from joint inversion and quantitative interpretation of seismic and gravity data. J. Geophys. Res.: Solid Earth 124, 11170–11191. http://dx.doi.org/10.1029/2019JB018476.

Petersen, T., Gledhill, K., Chadwick, M., Gale, N.H., Ristau, J., 2011. The New Zealand national seismograph network. Seismol. Res. Lett. 82, 9–20.

Rawlinson, N., Spakman, W., 2016. On the use of sensitivity tests in seismic tomography. Geophys. J. Int. 205, 1221–1243. http://dx.doi.org/10.1093/gji/ggw084.

Reyners, M., Eberhart-Phillips, D., Stuart, G., Nishimura, Y., 2006. Imaging subduction from the trench to 300 km depth beneath the central North Island, New Zealand, with Vp and Vp/Vs. Geophys. J. Int. 165, 565–583. http://dx.doi.org/10.1111/j.1365-246X.2006.02897.x.

Reyners, M., Stuart, G., 2002. The central north island passive seismic experiment. In: Institute of Geological & Nuclear Sciences Science Report.

Rosenberg, M.D., 2017. Volcanic and Tectonic Perspectives on the Age and Evolution of the Wairakei–Tauhara Geothermal System. Doctoral dissertation. Te Herenga Waka - Victoria University of Wellington.

Rosenberg, M.D., Wilson, C.J.N., Bignall, G., Ireland, T.R., Sepulveda, F., Charlier, B.L.A., 2019. Structure and evolution of the Wairakei–Tauhara geothermal system (Taupo Volcanic Zone, New Zealand) revisited with a new zircon geochronology. J. Volcanol. Geotherm. Res. 390, 106705. http://dx.doi.org/10.1016/j.jvolgeores.2019.106705.

Rowland, J.V., Simmons, S.F., 2012. Hydrologic, magmatic, and tectonic controls on hydrothermal flow, Taupo Volcanic Zone, New Zealand: Implications for the formation of epithermal vein deposits. Econ. Geol. 107, 427–457.

Sanders, C.O., Ponko, S.C., Nixon, L.D., Schwartz, E.A., 1995. Seismological evidence for magmatic and hydrothermal structure in Long Valley caldera from local earthquake attenuation and velocity tomography. J. Geophys. Res. 100, 8311–8326. http://dx.doi.org/10.1029/95JB00152.

Seebeck, H., Nicol, A., Villamor, P., Ristau, J., Pettinga, J., 2014. Structure and kinematics of the Taupo Rift, New Zealand. Tectonics 33, 1178–1199. http://dx.doi.org/10.1002/2014TC003569.

Sepulveda, F., Andrews, J., Alvarez, M., Montague, T., Mannington, W., 2013. Overview of deep structure using microseismicity at wairakei. In: 35th New Zealand Geothermal Workshop, Rotorua, New Zealand.

Sepulveda, F., Andrews, J., Kim, J., Siega, C., Milloy, S.F., 2015. Spatial–temporal characteristics of microseismicity (2009–2014) of the Wairakei Geothermal Field, New Zealand. In: World Geothermal Congress 2015, Melbourne, Australia.

Sepulveda, F.R., Siega, C., Bixley, P.F., Mannington, W.I., Milloy, S.F., Soengkono, S., Andrews, J., 2014. Wairakei geothermal field boundary: insights from recent geophysics and reservoir information. In: 39th Workshop on Geothermal Reservoir Engineering. Stanford University, Stanford, California.

Sewell, S.M., Cumming, W., Bardsley, C.J., Winick, J., Quinao, J., Wallis, I.C., Sherburn, S., Bourguignon, S., Bannister, S., 2015. Interpretation of microearthquakes at the Rotokawa geothermal field, 2008 to 2012. In: World Geothermal Congress 2015, Melbourne, Australia.

Sherburn, S.B., Bibby, H., 2003. Seismic velocity structure of the central Taupo Volcanic Zone, New Zealand, from local earthquake tomography. J. Volcanol. Geotherm. Res. 122, 69–88. http://dx.doi.org/10.1016/S0377-0273(02)00470-5.

Sherburn, S., Bromley, C., Bannister, S., Sewell, S., Bourguignon, S., 2015a. New Zealand geothermal induced seismicity: an overview. In: Proceedings World Geothermal Congress.

Sherburn, S., Sewell, S.M., Bourguignon, S., Cumming, W., Bannister, S., Bardsley, C., Winick, J., Quinao, J., Wallis, I.C., 2015b. Microseismicity at Rotokawa geothermal field, New Zealand, 2008–2012. Geothermics 54, 23–34. http://dx.doi.org/10.1016/j.geothermics.2014.11.001.

Smithies, S.L., Gravley, D.M., Gualda, G.A.R., 2024. Connecting the dots: the lava domes' perspective of magmatism related to an ignimbrite flare-up. J. Petrol. 65, http://dx.doi.org/10.1093/petrology/egad090.

Smithies, S.L., Harmon, L.J., Allen, S.M., Gravley, D.M., Gualda, G.A., 2023. Earth Planet. Sci. Lett. 607, 118053.

Stagpoole, V., Miller, C., Tontini, F.C., Brakenrig, T., 2020. A two million-year history of rifting and caldera volcanism imprinted in new gravity anomaly compilation of the Taup Volcanic Zone, New Zealand. N. Z. J. Geol. Geophys. 1–14. http://dx.doi.org/10.1080/00288306.2020.1848882.

Stern, T., Benson, A., 2011. Wide-angle seismic imaging beneath an andesitic arc: Central North Island, New Zealand. J. Geophys. Res.: Solid Earth 116, http://dx.doi.org/10.1029/2011JB008337.

Tarantola, A., Valette, B., 1982. Generalized nonlinear inverse problems solved using the least squares criterion. Rev. Geophys. 20, 219–232.

Thurber, C.H., 1983. Earthquake locations and three-dimensional crustal structure in the Coyote Lake area, central California. J. Geophys. Res.: Solid Earth 88, 8226–8236.

Tryggvason, A., Rögnvaldsson, S.T., Flóvenz, O.G., 2002. Three-dimensional imaging of the P-and S-wave velocity structure and earthquake locations beneath southwest Iceland. Geophys. J. Int. 151, 848–866.

Uieda, L., Tian, D., Leong, W.J., Toney, L., Schlitzer, W., Grund, M., Newton, D., Ziebarth, M., Jones, M., Wessel, P., 2021. PyGMT: A Python interface for the Generic Mapping Tools, zenodo. http://dx.doi.org/10.5281/ZENODO.4522136.

Ulberg, C.W., Creager, K.C., Moran, S.C., Abers, G.A., Thelen, W.A., Levander, A., Kiser, E., Schmandt, B., Hansen, S.M., Crosson, R.S., 2020. Local source Vp and Vs tomography in the Mount St, Helens region with the iMUSH broadband array. Geochem. Geophys. Geosystems 21, http://dx.doi.org/10.1029/2019GC008888.

Um, J., Thurber, C., 1987. A fast algorithm for two-point seismic ray tracing. Bull. Seismol. Soc. Am. 77, 972–986.

Vesnaver, A., Böhm, G., 2000. Staggered or adapted grids for seismic tomography? Lead. Edge 19, 944–950. http://dx.doi.org/10.1190/1.1438762.

Villamor, P., Berryman, K., 2001. A late quaternary extension rate in the Taupo Volcanic Zone, New Zealand, derived from fault slip data. N. Z. J. Geol. Geophys. 44, 243–269. http://dx.doi.org/10.1080/00288306.2001.9514937.

Villamor, P., Berryman, K.R., Ellis, S.M., Schreurs, G., Wallace, L.M., Leonard, G.S., Langridge, R.M., Ries, W.F., 2017. Rapid evolution of subduction-related continental intraarc rifts: The Taupo Rift, New Zealand. Tectonics 36, 2250–2272. http://dx.doi.org/10.1002/2017TC004715.

Waldhauser, F., Ellsworth, W.L., 2000. A double-difference earthquake location algorithm: Method and application to the northern Hayward fault, California. Bull. Seismol. Soc. Am. 90, 1353–1368.

Wallace, L.M., Beavan, J., McCaffrey, R., Darby, D., 2004. Subduction zone coupling and tectonic block rotations in the North Island, New Zealand. J. Geophys. Res.: Solid Earth 109.

Wallis, I., Bardsley, C., Powell, T., Rowland, J., OBrien, J., 2013. A structural model for the Rotokawa geothermal field, New Zealand. In: 35th New Zealand Geothermal Workshop: 2013 Proceedings, Rotorua, New Zealand.

Williams, C.A., EberhartPhillips, D., Bannister, S., Barker, D.H., Henrys, S., Reyners, M., Sutherland, R., 2013. Revised interface geometry for the Hikurangi subduction zone, New Zealand. Seismol. Res. Lett. 84, 1066–1073.

Wilson, C.J.N., 1993. Stratigraphy, chronology, styles and dynamics of late Quaternary eruptions from Taupo volcano, New Zealand. Philos. Trans. R. Soc. Lond. Ser. A: Phys. Eng. Sci. 343, 205–306.

Wilson, C.J., Gravley, D., Leonard, G., Rowland, J., 2009. Volcanism in the central Taupo Volcanic Zone, New Zealand: tempo, styles and controls. In: Studies in Volcanology: The Legacy of George Walker. vol. 2, Special Publications of IAVCEI, pp. 225–247.

Wilson, C.J.N., Houghton, B.F., McWilliams, M.O., Lanphere, M.A., Weaver, S.D., Briggs, R.M., 1995. Volcanic and structural evolution of Taupo Volcanic Zone, New Zealand: a review. J. Volcanol. Geotherm. Res. 68, 1–28. http://dx.doi.org/10.1016/0377-0273(95)00006-G.

Wu, R.S., Aki, K., 1988. Introduction: Seismic wave scattering in three-dimensionally heterogeneous earth. In: Scattering and Attenuations of Seismic Waves, Part I. Springer, pp. 1–6.

Zhang, H., Thurber, C.H., 2003. Double-difference tomography: The method and its application to the Hayward Fault, California. Bull. Seismol. Soc. Am. 93 (5), 1875–1889.

Zhang, H., Thurber, C., 2006. Development and applications of double-difference seismic tomography. Pure Appl. Geophys. 163, 373–403.

Zhang, H., Thurber, C., Bedrosian, P., 2009. Joint inversion for Vp Vs, and Vp/Vs at SAFOD, Parkfield, California. Geochem. Geophys. Geosystems 10, http://dx.doi.org/10.1029/2009GC002709.

Zhu, W., McBrearty, I.W., Mousavi, S.M., Ellsworth, W.L., Beroza, G.C., 2022. Earthquake phase association using a bayesian gaussian mixture model. J. Geophys. Res. 127 (5), E2021JB023249.